

Optoelectronic multifunctionality of combustion-activated fluorine-doped tin oxide films with high optical transparency



Bon-Ryul Koo^a, Ju-Won Bae^b, Hyo-Jin Ahn^{a,b,*}

^a Program of Materials Science & Engineering, Convergence Institute of Biomedical Engineering and Biomaterials, Seoul National University of Science and Technology, Seoul, 01811, Republic of Korea

^b Department of Materials Science and Engineering, Seoul National University of Science and Technology, Seoul, 01811, Republic of Korea

ARTICLE INFO

Keywords:

Films
Electrical properties
Optical properties
Transition metal oxides
Optoelectronic devices

ABSTRACT

As transparent conducting oxides (TCOs) have been widely used as a common component of many optoelectronic applications, ensuring high conductivity and transparency TCOs has become a pivotal concern. In the present study, we report developing the combustion-activated pyrolysis route of horizontal ultrasonic spray pyrolysis deposition (HUSPD) as a novel strategy to form highly transparent conducting fluorine-doped tin oxide (FTO) films. Compared to the basic route, the combustion-activated FTO films showed an attractive transparent conducting performance (figure of merit of $5.34 \times 10^{-2} \Omega^{-1}$) with a highly improved optical transparency (90.1%) due to the formation of a smooth and dense film structure to reduce light scattering on the surface, and a decrease of oxygen vacancies to broaden the optical bandgap, all of which yielded an excellent performance as compared to the previously reported studies on the FTO films. Moreover, when the combustion-activated FTO films were used as TCOs of electrochromic devices and dye-sensitized solar cells, they acquired multifunctional effects of (a) an efficient electron transfer by (200) preferred orientations of the FTO; (b) a relaxed light scattering on the interface due to smooth and dense surface morphology of the FTO films; and (c) a broad optical bandgap by decreased oxygen vacancies, resulting in an impressive improvement of both electrochromic and photovoltaic performances. Taken together, our results demonstrate that combustion-activated FTO films are an attractive technique for forming high-performance TCOs that can further be used in multifunctional optoelectronic devices.

1. Introduction

Transparent conducting oxides (TCOs) are a type of film structure based on metal oxides with a wide bandgap exceeding 3 eV (tin-doped indium oxide (ITO), aluminum-doped zinc oxide (AZO), and fluorine-doped tin oxide (FTO)). Due to their unique characteristics of low resistivity ($< 10^{-4} \Omega \text{ cm}$) and high optical transparency ($> 80\%$), TCOs play a key role in wide array of optoelectronic applications, such as smart windows, touch screens, displays (e.g., liquid crystal displays (LCD) and organic light emitting diode displays), and solar cells [1–5]. Until now, ITO has been considered as the industrial standard of the TCOs; however, there are several intrinsic problems of ITO, such as striking absorption in the near-IR region, scarce indium on earth, and high mechanical brittleness, which make its performance unsatisfactory for the applications [6,7]. Therefore, there have been many research efforts to develop a potential alternative to ITO. As one of these

alternatives, FTO, which offers several advantages such as low cost, good thermal and chemical stability, and competitive transparent conducting performances [8], has recently received a considerable scholarly attention in terms of its use in electrochromic devices (ECDs) or dye-sensitized solar cells (DSSCs).

Globally, as most energy use (ca. 41%) is based on the unique capacity to maintain comfortable light for energy-saving or to storage incident light for energy generation, the importance of optoelectronic devices has expanded and their market has been continuously growing [9]. Recently, electrochromic devices (ECDs) have been noted as an optoelectronic technique with attractive functions for their applications in light-modulating devices or information displays, such as smart windows, chemical sensors, electronic displays, and switchable mirrors [10–13]. Interestingly, the smart windows are potential candidates to save energy by reducing heating or cooling loads through the technique controlling the amount of solar heat entering indoor spaces [9]. That is,

* Corresponding author. Program of Materials Science & Engineering, Convergence Institute of Biomedical Engineering and Biomaterials, Seoul National University of Science and Technology, Seoul, 01811, Republic of Korea.

E-mail address: hjahn@seoultech.ac.kr (H.-J. Ahn).

<https://doi.org/10.1016/j.ceramint.2019.02.080>

Received 5 December 2018; Received in revised form 7 February 2019; Accepted 12 February 2019

Available online 14 February 2019

0272-8842/ © 2019 Elsevier Ltd and Techna Group S.r.l. All rights reserved.

the ECDs can reversibly and persistently control universal optical properties (transparency, absorption, reflection, and color) by means of a small electric field causing a variation of electronic structure on electrochromic (EC) materials by electron-ion behavior and have unique advantages of low operating voltage and low memory effect [14]. Typically, the components of the ECD structure are five functional layers with two TCOs, two different EC materials, and ion conductor that is strongly related to the performance of the ECDs, such as optical modulation, coloration efficiency (CE), and switching speed. In addition, DSSCs are a powerful optoelectronic application to generate electricity using the principle of photosynthesis, and offer the unique advantages of flexibility, simple device structure, and various applications [15,16]. For DSSCs, they generally consist of two TCOs, TiO₂ working electrode with sensitizing dyes, Pt counter electrodes, and the iodide electrolyte [17]. Interestingly, it is noted that common TCO of the ECDs and DSSCs uses the FTO films. Moreover, the FTO films are an indispensable component of a wide variety of optoelectronic applications, because they can perform important assignments that materialize the transparency of the devices and transport the formed electrons to external circuit, thereby determining the performance of the optoelectronic applications [18]. Despite this fact, however, research using the FTO films to expand the application of optoelectronic devices remains scarce thus far [19–21].

To extensively use the FTO films for optoelectronic devices, the following fundamental features are required: a low sheet resistance to increase electron transport and a high optical transmittance to relax an optical scattering or loss, which is mainly related to crystallographic structures and defect structures of the formed FTO films. Numerous reports are available that proposed the ways to obtain the high-performance FTO films by delicately controlling these structures through various deposition techniques, including pulsed laser deposition, chemical vapor deposition, sputtering, spin-coating, and ultrasonic spray pyrolysis deposition (USPD) [21–25]. Commercially, it is known that the FTO films (TEC8, Pilkington) fabricated by an atmospheric pressure chemical vapor deposition using inert gas (99.99%) have been used as the representative TCO. However, due to the use of inert gas during the FTO deposition, the resultant FTO films show a high haze property, whereas they tend to have a low optical transmittance, which can be limited in practical use of the optoelectronic applications [26,27]. Recently, the USPD to simply and cost-efficiently fabricate film structure using precursor droplets with the size of 1–100 μm generated from ultrasonic atomization have been highlighted as a powerful deposition technique for high-performance FTO films [28]. In particular, this technique makes it possible to accurately adjust the morphological, structural, and chemical properties of the formed FTO films by controlling the conditions of the precursor solution (e.g., precursor, solvents, and additives, etc.) and deposition parameters (e.g., process time, flow rate, ultrasonic amplitude, temperature, and carrier gas, etc.), thereby leading to the selective implementation of their transparent conducting performances [29–31]. For example, increasing fluorine content to tin in the FTO films using the USPD caused a decrease of resistivity or sheet resistance due to the increased effect of F doping [29]. In addition, a study on the solvent-dependent growth of sprayed FTO films using methanol, ethanol, propane-2-ol, and distilled water demonstrated that the samples fabricated by propane-2-ol have the lowest sheet resistance owing to the increasing amount of F species as the result of a decrease in the evaporation rate of the solvent [31]. Although various approaches have been reported, most of the research that targets high-performance FTO films appears to be focused on obtain low sheet resistance or resistivity for the optimized transparent conducting performances, whereas there is a drastic decline of their optical transmittance due to light scattering by the increased carrier concentration. Therefore, getting a highly transparent performance and maintaining a low sheet resistance remains a major challenge in the context of the requirement of the growing performance of optoelectronic applications.

In the present study, we report a novel strategy for forming highly transparent conducting FTO films using the combustion-activated pyrolysis route of horizontal ultrasonic spray pyrolysis deposition (HUSPD). The combustion route can generate the energy-efficient fabrication of materials, leading to a supply of localized energy to synthetic product, which is only used in chalcogenides, carbides, and III–V semiconductors [32–34]. This route enables fabrication of high-performance FTO films and ensures a high optical transparency. In addition, our results suggest that tuning of the FTO films by the combustion-activated pyrolysis route considerably improves the performance of both ECDs and DSSCs and show the investigation of mechanism improving performance of the optoelectronic devices with highly transparent FTO films, yielding the broaden applications of the FTO films on the optoelectronic devices.

2. Experimental

In the present study, combustion-activated FTO films were fabricated by the HUSPD using combustion-activated pyrolysis route. The precursor solution was prepared by dissolving 0.68 M tin chloride pentahydrate (SnCl₄·5H₂O, SAMCHUN) and ammonium fluoride (NH₄F, Aldrich) into a mixture consisting of 95 vol % de-ionized (DI) water and 5 vol% ethyl alcohol (C₂H₅OH, Duksan). To obtain the optimum performance of the FTO films, the mole ratio of F/Sn in the precursor solution was fixed to 1.765. Then, combustion activators of ammonium nitrate (NH₄NO₃, Aldrich)/urea (NH₂CONH₂, Aldrich) with the molar ratio of 1 were added to the solution described above. In the next step, in order to optimize the combustion-activated pyrolysis route for forming the FTO films, the weight ratio of combustion activators to tin precursor was controlled to 0, 10, 15, and 20 wt% (herein named as bare FTO, CA10-FTO, CA15-FTO, and CA20-FTO, respectively). After stirring, the transparent precursor solutions were sprayed through the ultrasonic atomizer (1.6 MHz) onto a glass substrate (Corning EAGLE XG™). During the FTO deposition, the solution was made flow at the speed of 15 L/min through air gas under the substrate rotation speed of 5 rpm, and the deposition temperature and time were maintained at 420 °C and 23 min, respectively. After the deposition, the films were allowed to cool down naturally, and the combustion-activated FTO films were obtained through the HUSPD.

The evaluation of the electrochromic (EC) performances of the films was performed by using the WO₃ films as a coating EC material for the combustion-activated FTO films. To prepare the WO₃ films, 10 wt% tungsten (VI) chloride (WCl₆, Aldrich) were dissolved into in 2-propanol ((CH₃)₂CHOH, Aldrich). After stirring, the resultant WCl₆ solution was spin-coated at 2000 rpm for 30s on the FTO films and then annealed at 300 °C in air to form WO₃ films.

To measure the photovoltaic performances of the combustion-activated FTO films, we used the dye-sensitized solar cells (DSSCs) with the working and counter electrodes. The TiO₂ paste for the working electrode was prepared by mixing P25 (DEGUSSA), acetylacetone (C₅H₈O₂, Aldrich), hydroxypropyl cellulose (HCP, *M_w* = 80,000 g/mol, Aldrich) into deionized water, which was squeeze-printed on the combustion-activated FTO films. After annealing at 500 °C, the dye absorption was performed by immersing the TiO₂ paste-coated FTO films into the 0.5 mM N719 (Ru(dcbpy)₂(NCS)₂, Solaronix) dye solution for 24 h in a dark room. For preparation of the counter electrodes, a 5 mM Pt solution with chloroplatinic acid hexahydrate (H₂PtCl₆·6H₂O, Aldrich) and 2-propanol ((CH₃)₂CHOH, Aldrich) was coated onto the combustion-activated FTO films using the spin coating method; then the solution was annealed at 450 °C for 30 min. Finally, the assembly of the DSSCs was carried out by overlapping the working and counter electrodes as sandwich-type cells, where 0.6 M BMII (1-Butyl-3-methylimidazolium iodide)-based iodine solution used as an electrolyte was filled into the narrow space between the two electrodes.

The thermal behavior was traced by differential scanning calorimetry (DSC, DSC-60, Shimadzu). The structural and chemical

properties were characterized by X-ray diffraction (XRD, Rigaku D/Max-2500 diffractometer using Cu K_{α} radiation), X-ray photoelectron spectroscopy (XPS, AXIS ultra-delay line detector equipped with an Al K_{α} X-ray source, KBSI Daedeok Headquarters), and Fourier transform infrared (FTIR) spectroscopy (Thermo Fisher Scientific, Nicolet iS50). The observation of surface morphology was performed by field-emission scanning electron microscopy (FESEM, Hitachi S-4800) and atomic force microscopy (AFM, diDimension™ 3100). The measurement of refractive index in the range of 300–1000 nm was performed using a spectroscopic ellipsometer (Woollam, M2000D). The electrical and optical properties were measured by the Hall-effect measurement system (Ecopia, HMS-3000) and ultraviolet-visible (UV-vis) spectroscopy (Perkim-Elmer, Lambda-35), respectively. The electrochemical and EC performances were analysed using a potentiostat/galvanostat (PGSTAT302N, FRA32M, Metrohm Autolab B.V., The Netherlands) together with ultraviolet-visible (UV-vis) spectroscopy (Perkim-Elmer, Lambda-35). The evaluation of the photovoltaic performances using the DSSCs was performed using a solar simulator equipped with a 150 W Xenon arc lamp.

3. Results and discussion

In the fabrication of the combustion-activated FTO films using the HUSPD, an important process would be a pyrolysis of precursors to change the FTO characteristics related to their transparent conducting performances [12,30]. The precursors used in the basic pyrolysis route of the HUSPD have a $[\text{Cl}_3(\text{H}_2\text{O})\text{Sn}(\text{OH})]$ structure with two Sn^{4+} ions surrounded by three Cl, one OH, and one H_2O ligand by the use of $\text{SnCl}_4 \cdot 5\text{H}_2\text{O}$, which requires a high activation energy to convert the precursors into the crystalline FTO to the FTO films due to its hygroscopic characteristic [35]. On the other hand, in the present study, we propose a novel combustion-activated pyrolysis route to form the crystalline FTO by using ammonium nitrate as an oxidizer and urea as a fuel. Interestingly, this route enables lowering of activation energy to form the crystalline FTO due to self-generated energy by exothermic reaction. Therefore, to demonstrate the mechanism of the combustion-activated pyrolysis route, we performed the thermal analysis of the precursor solution for bare FTO, CA10-FTO, CA15-FTO, and CA20-FTO using the DSC. As shown in Fig. 1a, all samples mainly exhibited an endothermic peak and two exothermic peaks. A broad endothermic peak at 25–130 °C was due to the elimination of physisorbed solvents in the precursor solutions. The minor endothermic peak observed at 190–210 °C could originate from the pyrolysis of NH_4F used as the doping source of the FTO [36]. In particular, the major exothermic peak emitted in the range of 210–290 °C shows a noticeable difference among the samples, which is related to the pyrolysis of Sn precursor for forming the crystalline FTO used as the main matrix of the FTO films [37]. For bare FTO, there was an endothermic peak centered at 275 °C. Compared to bare FTO, the endothermic peaks of the samples using the combustion-activated pyrolysis route showed a lower temperature. Specifically, with an increase of the weight ratio of the combustion activators in the precursor solution, the temperature of the endothermic peak decreased from 241 °C for CA10-FTO to 233 °C for CA15-FTO, and then increased to 254 °C for CA20-FTO, meaning that CA15-FTO has highly accelerated the effect of combustion-activated pyrolysis as compared to the other samples. This phenomenon is also confirmed by the enthalpy value of the samples calculated from the endothermic peak at 210–290 °C of the DSC curve (see Fig. 1b). In the Arrhenius law, the activation energy quantity (E_a) analogous to the enthalpy quantity (ΔH) is an important factor that affects the nucleation-and-growth process of materials. Therefore, according to Chen et al. and Phuoc et al., with a decrease of the activation energy quantity, the particle size of the resultant materials decreases (see Eq. (1–3)) [38,39]:

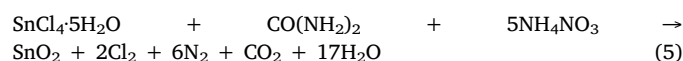
$$E_a = \Delta H + RT \quad (1)$$

$$E_d/E_{\infty} = [1 - (1 - Z_d/Z_{\infty})N_s/N_t] \quad (2)$$

$$N_s/N_t = 4f_s/f_v(d_p/d_a) + 2f_s \quad (3)$$

where R is the gas constant, T is temperature, E_d is the size-dependent activation energy, E_{∞} is the activation energy of the bulk material, N_s is the number of the surface atoms, N_t is the total atoms, d_p is the diameter of nanoparticles, and d_a is the atom diameter. Such behavior of the particle size among the samples is confirmed from the SEM results obtained by annealing the precursor solutions of the samples at 300 °C (see Fig. S1). As a result, the combustion-activated pyrolysis route (see Fig. 1c) was successfully achieved due to the decrease of the activation energy quantity by self-generated energy, which can act as the main driving force resulting in the highly developed transparency of the FTO films to improve the performances of optoelectronic devices.

Fig. 2a shows the XRD patterns of bare FTO, CA10-FTO, CA15-FTO, and CA20-FTO to investigate the effect of the combustion-activated pyrolysis route on the crystal structure. The XRD patterns consist of characteristic peaks at 2θ values of 26.51° for the (110) plane, 33.85° for the (101) plane, 37.90° for the (200) plane, and 51.72° for the (211) plane. These peaks are consistent with a tetragonal rutile FTO phase [28]. Interestingly, there was an impressive difference of intensity ratio between the (200) and (110) planes among the samples. With an increase of the weight ratio of combustion activators, the intensity ratio of the (200)/(110) planes gradually enhanced from 1.85 for bare FTO to 4.68 for CA15-FTO, and then decreased to 1.41 when the weight ratio of combustion activators reached 20 wt%. This result means that CA15-FTO possesses the dominant (200) preferred orientations among the samples. In general, the SnO_2 of tetragonal crystal structure has the preferred orientations of (110) together with presence of other peaks, such as (101), (211), and (310). However, consistently with the previous reports, with the addition of HCl or NH_4F in the Sn precursor solution, a drastic growth of (200) orientations is promoted due to the growth relaxation of {101} twin planes corresponding to the corner of the SnO_2 crystallites by the generation of gases during the film deposition [40–42]. On the other hand, as compared to the basic pyrolysis route of SnO_2 (see Eq. (4)), the combustion-activated pyrolysis route can generate a large amount of gases, such as Cl_2 , N_2 , CO_2 , and H_2O for forming the SnO_2 (see Eq. (5)) [43,44].



The growth of (200) preferred orientations is parallel to the glass substrate, implying better electronic transport properties of the FTO films for their use in various optoelectronic applications [28,45]. The results of the XPS analysis confirmed the chemical binding states of the FTO films with the effect of the combustion-activated pyrolysis route. As shown in Fig. 2b, asymmetric Sn 3d spectra of all samples were consistently divided into two characteristic peaks of Sn–Sn related to Sn^{4+} of the SnO_2 phase (486.6 eV for Sn 3d_{5/2} and 495.1 eV for Sn 3d_{3/2}) and Sn–F corresponding to F-substitution in the SnO_2 phases (487.7 eV for Sn 3d_{5/2} and 496.3 eV for Sn 3d_{3/2}) [46,47]. It is clear that the use of combustion-activated pyrolysis route induced no critical change of the position and area of Sn 3d spectra. However, from O 1s spectra shown in Fig. 2c, the area ratio (0.52 for bare FTO, 0.32 for CA10-FTO, 0.28 for CA15-FTO, and 0.24 for CA20-FTO) of V_o (532.0 eV) to Sn–O (530.4 eV) can be seen to decrease with an increase of the weight ratio of combustion activators, which can result from the increased effect of ammonium nitrate used as the oxidizer agent [48]. This is proved by a gradual increase of the O–Sn–O vibrational mode shown in the FTIR curve (see Fig. S2). Therefore, the striking change of V_o on the FTO films caused by the combustion-activated pyrolysis route can affect electrical and optical properties of the FTO films. As shown in Fig. 2d, we determined their optical bandgap (E_g) through the curves of $(ah\nu)^2$ versus photon energy ($h\nu$) calculated from the transmittance

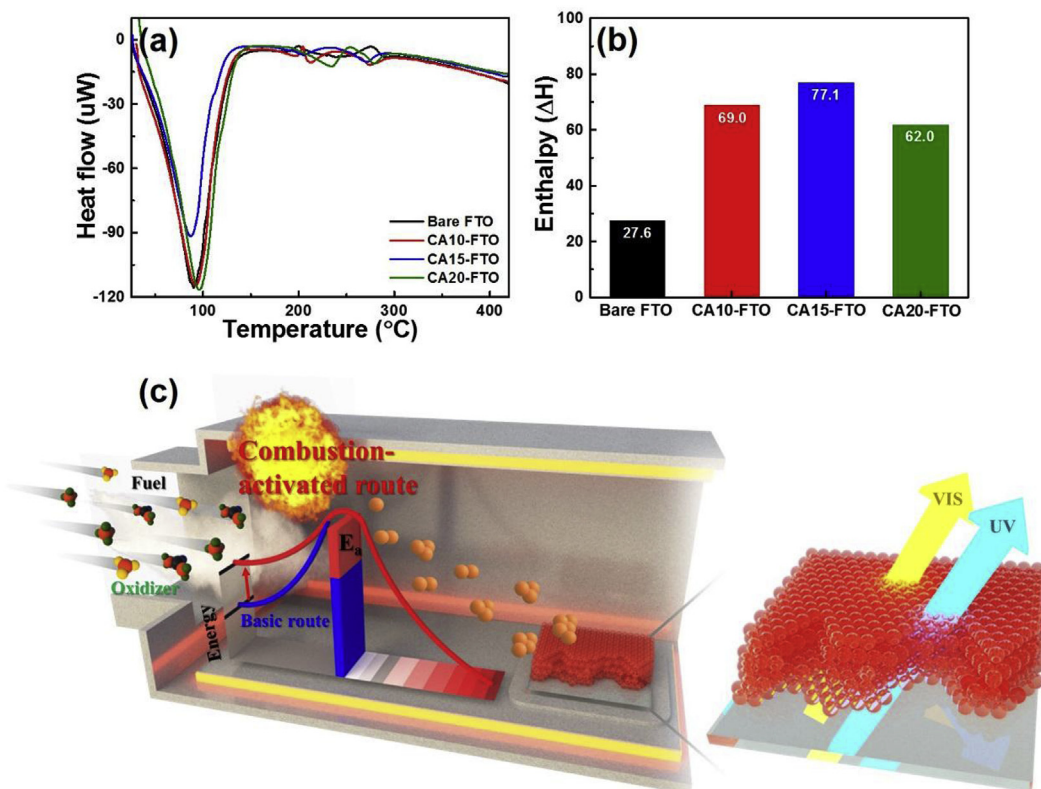


Fig. 1. (a) DSC curves measured from precursor solutions of bare FTO, CA10-FTO, CA15-FTO, and CA20-FTO in range from 25 to 420 °C at air atmosphere, (b) enthalpy values calculated at exothermic peak in range of 210–290 °C, and (c) schematic illustration for formation mechanism of highly transparent FTO films using combustion-activated pyrolysis route.

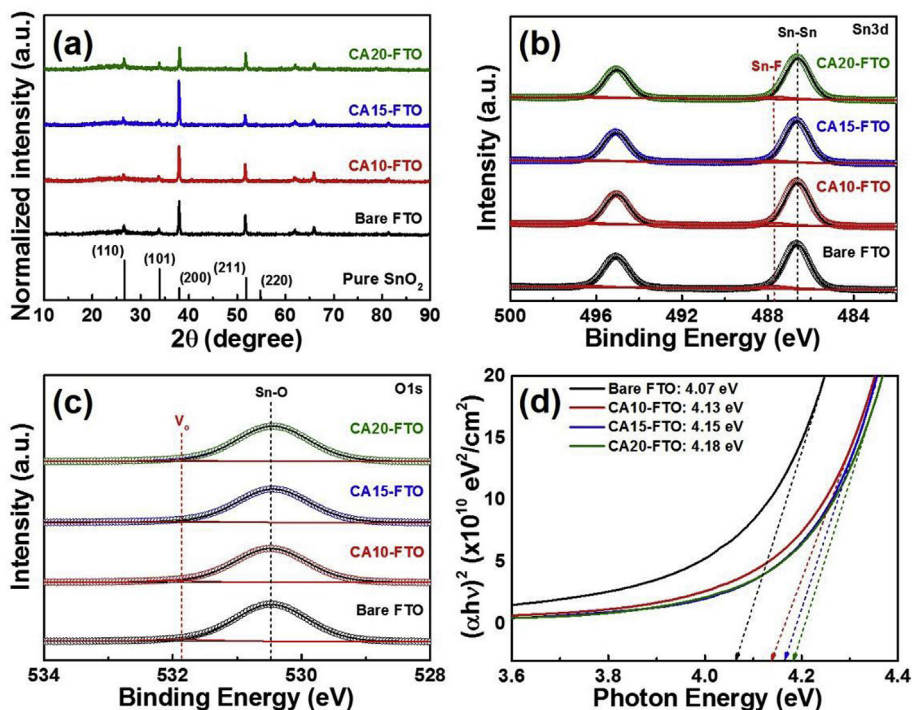


Fig. 2. (a) XRD patterns, XPS core-level spectra of (b) Sn 3d and (c) O 1s, and (d) curves of $(\alpha h\nu)^2$ versus photon energy obtained from all FTO films.

spectra of the samples using Eq. (6) [49]:

$$\alpha h\nu = A(h\nu - E_g)^n \tag{6}$$

where α , A , and n are the optical absorption coefficient, an energy-

independent constant, and constant, respectively. The calculated optical bandgap of bare FTO is 4.07 eV, which, as indicated in a previous report, corresponds to the general value of the FTO [28]. However, for the combustion-activated FTO films, there was a gradual increase of the

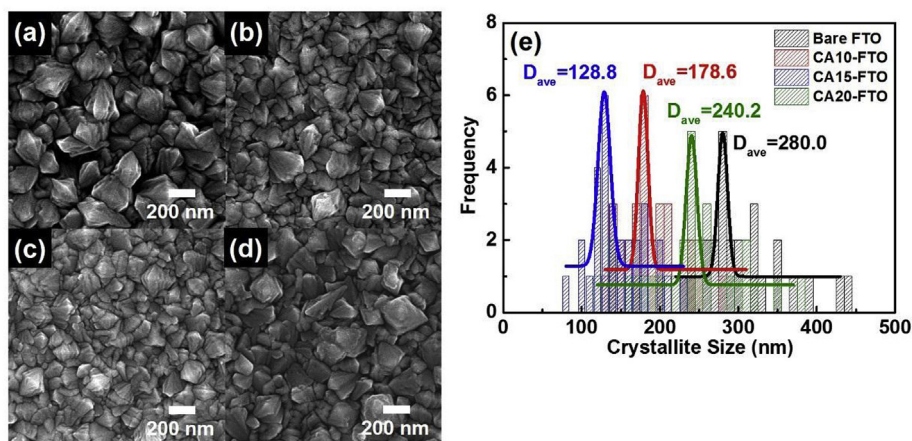


Fig. 3. Top-view FESEM images of (a) bare FTO, (b) CA10-FTO, (c) CA15-FTO, and (d) CA20-FTO and (e) distribution of crystallite size measured from all FTO films.

optical bandgap with an increase of the weight ratio of combustion activators, which had a higher value than that of bare FTO. This result can be due to the variation of the conduction band minimum (CBM) by the decreased oxygen vacancies. The relative position of the CBM can be determined by valence band maximum (VBM) determined from the valence-band XPS spectrum (see Fig. S3), in which the relative position of VBM with reference of the Fermi level (E_F , 0 eV) is defined by means of a linear extrapolation [50,51]. From this spectrum, the relative position of VBM revealed similar values among the samples. Based on the calculated VBM and optical bandgap, we can predict the relative position of the CBM by calculating $CBM-E_F$ (3.55 eV for bare FTO, 3.56 eV for CA10-FTO, 3.59 eV for CA15-FTO, and 3.59 eV for CA20-FTO), resulting in a gradual negative shift of the CBM. Therefore, the combustion-activated pyrolysis route can lead to widening of their optical bandgap due to the decrease of the oxygen vacancies created as the donor below conduction band, which is useful in terms of enhancing the optical transmittance of the FTO films to improve the performance of optoelectronic devices [51].

The surface morphology of all FTO films was characterized by the FESEM (see Fig. 3). The top-view FESEM images clearly show the film structures with interlocked crystallites throughout the entire surface; however, there is a remarkable difference of the surface morphology and crystallite size among the samples. For bare FTO (see Fig. 3a), the rough surface morphology with partial pinholes between the crystallites was observed, which can be attributed to the wide crystallite size distribution in the range of 217.5–423.7 nm (see Fig. 3e). Interestingly, the crystallite sizes of the FTO films fabricated by the combustion-activated pyrolysis route were smaller than those of bare FTO and were found to decrease from CA10-FTO (123.2–300.1 nm, see Fig. 3b) to CA15-FTO (74.8–226.4 nm, see Fig. 3c), which is due to the effect of the increasing enthalpy by self-generated energy, resulting in the formation of a smooth and dense surface morphology without pinholes [37]. However, for CA20-FTO (see Fig. 3d), it can be observed that the crystallite size (217.5–381.3 nm) increased as compared to CA15-FTO; this increase occurred despite the high weight ratio of combustion activators induced by the aggregation of the FTO crystallites by an excessive amount of urea corresponding to organic source [52], thus showing a rough surface morphology with partial pinholes. This variation of the surface morphology among the samples is convincingly confirmed by the AFM results (see Fig. S4). In addition, the formation of a smooth and dense film structure is clearly confirmed by the curve of refractive index (n) of bare FTO and CA15-FTO (see Fig. 4). This curve indicates that the refractive index of CA15-FTO at the top part is higher than that of bare FTO, while there was a similar refractive index at the bottom part of the FTO films. This noticeable increase may be due to an improved densification with a decrease of the growing FTO particle size by the effect of combustion-activated pyrolysis route, as proved by the FESEM images

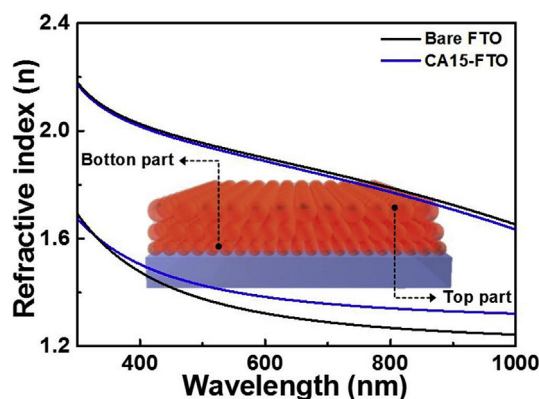


Fig. 4. Curve of refractive index in wavelength range of 300–1000 nm obtained from top and bottom parts of bare FTO and CA15-FTO, respectively.

of the FTO films fabricated at different deposition times of the HUSPD (see Fig. S5). Therefore, the reduction of the refractive index difference between the bottom and top parts of the FTO films can be seen to be an important factor to improve their optical transmittance (T) by declining light reflectance (R) (see Eq. (7–8)) [53]:

$$T = 1 - R \quad (7)$$

$$R = (n_1 - n_2/n_1 + n_2)^2 \quad (8)$$

Taken together, the results outlined above demonstrate that the combustion-activated pyrolysis route can result in the fabrication of a smooth and dense surface morphology of the FTO films (CA15-FTO).

Electrical properties such as the carrier concentration, Hall mobility, and resistivity of all FTO films were measured using the Hall effect measurement system and are shown in Fig. 5a. When the weight ratio of the combustion activators increased, the value of carrier concentration gradually decreased from $4.49 \times 10^{20} \text{ cm}^{-3}$ for bare FTO to $3.87 \times 10^{20} \text{ cm}^{-3}$ for CA20-FTO. This result can be due to the decreased oxygen vacancies in the FTO films, as confirmed by the XPS and FTIR results (see Fig. 2c and S2, respectively) [48]. Interestingly, a major increase of Hall mobility from $35.2 \text{ cm}^2/(\text{V s})$ for bare FTO to $42.8 \text{ cm}^2/(\text{V s})$ for CA15-FTO is observed. This result can mainly be attributed to the dominant growth of the (200) preferred orientations on the FTO films. According to reports of Messad et al. and Agashe et al., the FTO films with the (200) preferred orientations can cause the formation of a smooth and dense film structure, corresponding to the SEM and AFM results in our study (see Fig. 3c and S4c, respectively), which is useful to improve Hall mobility as the result of the decreased carrier scattering at the grain boundaries and surface [35,45].

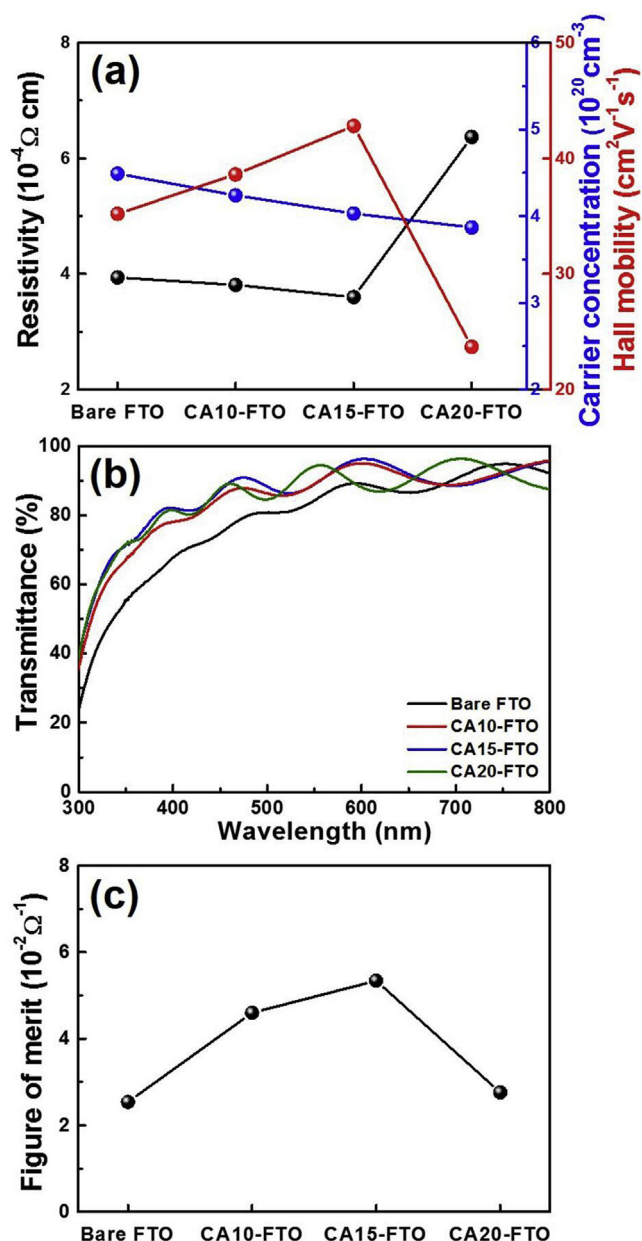
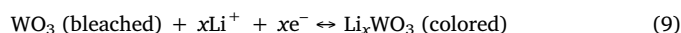


Fig. 5. (a) Electrical properties, (b) optical transmittance spectra in wavelength range of 300–800 nm, and (c) the resultant FOM of all FTO films.

Therefore, by considering the carrier concentration (N) and Hall mobility (μ), the resistivity ($\rho = 1/(Ne\mu)$) and sheet resistance of the FTO films were calculated (see Table S1 for a summary). Fig. 5b shows the spectra of the optical transmittances on the FTO films. It can be seen that the average optical transmittance in the wavelength range of 400–800 nm is 84.5% for bare FTO, 89.3% for CA10-FTO, 90.1% for CA15-FTO, and 89.1% for CA20-FTO. The outstanding optical transmittance of the FTO films (CA15-FTO) can mainly be attributed to the effect of the combustion-activated pyrolysis route that has the following

two favorable characteristics: (i) a smooth and dense film structure of FTO to relax light scattering on the surface and (ii) a wide optical bandgap to permit the light transmission [28,54]. Therefore, to predict their transparent conducting performance, we calculated a figure of merit (FOM, $\phi = T^{10}/R_{\text{sh}}$) using the average optical transmittance (T) and the sheet resistance (R_{sh}) [28]. As can be seen in Table 1, the FOM value of CA15-FTO was the highest among the samples due to their good sheet resistance ($6.6 \pm 0.30 \Omega/\square$) and excellent optical transmittance (90.1%) resulting from the optimum combustion-activated pyrolysis route. This optical transmittance is clearly surpassing reported in previous studies on high-performance FTO electrodes (see Table S2) and is clearly confirmed from the comparison of the photographs between CA15-FTO and bare FTO (see Fig. S6).

To characterize the electrochromic performance of the FTO films, the CV measurement was performed by using WO_3 film as an EC material on the commercial FTO, bare FTO, and CA15-FTO. During the CV cycling in the range of -0.7 to 1.0 V, the samples showed a reversible color variation from deep blue in the colored state to transparent colorless in the bleached state (see Eq. (9)) [55]:



From the CV curves (see Fig. 6a), an improvement of both anodic and cathodic current densities for CA15-FTO ($6.6 \pm 0.30 \Omega/\square$), compared to those of the bare FTO ($7.3 \pm 0.30 \Omega/\square$) and the commercial FTO ($6.5 \pm 0.42 \Omega/\square$), can be observed; this improvement occurred despite no critical difference of sheet resistances. This finding implies that CA15-FTO can cause a large number of ions and electrons to diffuse and transfer into or out the WO_3 corresponding to enhancement of electrochemical activity to improve the EC performances, which can be attributed to the efficient electronic transport of the (200) preferred orientations on the FTO films, as proved by a better Hall mobility in the electrical properties (see Fig. 5a) [56,57]. The EC response of the FTO films was characterized by tracing the *in situ* optical transmittances in the colored (-0.7 V) and bleached states (1.0 V) for 60 s. The obtained curve (see Fig. 6b) offers two major EC performances of the transmittance modulation and switching speed (see Table 1 for a summary). For transmittance modulation defined as $\Delta T = T_b - T_c$, where T_b is transmittance in the bleached state and T_c is transmittance in the colored state, due to a high electrochemical activity increasing Li^+ intercalation and deintercalation, a wider transmittance modulation of CA15-FTO (60.6%), as compared to the bare FTO (55.8%) and the commercial FTO (52.6%), was observed. Specifically, widening of the transmittance modulation on CA15-FTO is also related to an increased transmittance in the bleached state, which results from a reduction of interfacial scattering between FTO and WO_3 by a smooth and dense surface morphology of the FTO films; this was confirmed by the diminished absorbance of CA15-FTO (see Fig. 6d). In particular, the switching speed (defined as the time to reach 90% of the entire transmittance modulation at 633 nm) is an important performance parameter in practical EC applications. Interestingly, despite no critical variation of sheet resistance, the switching speeds of CA15-FTO (9.5 s for the coloration speed and 6.9 s for the bleached speed) appear to be significantly improved as compared to other samples. This result can be due to the dominant growth of the (200) preferred orientations on the FTO films. That is, as the FTO films with the (200) preferred orientations provide an efficient electron transport, it can accelerate the electron diffusion at the interface between FTO and WO_3 films during

Table 1
Electrochromic and photovoltaic performances of optoelectronic devices using the FTO films.

	$\Delta T(\%)$	Coloration speed(s)	Bleached speed (s)	CE(cm^2/C)	V_{OC} (V)	J_{SC} (mA/cm^2)	ff(%)	$\eta(\%)$
Commercial FTO	52.6	12.1	12.5	39.4	0.71 ± 0.01	14.9 ± 0.51	58.4 ± 0.02	6.26 ± 0.25
Bare FTO	55.8	10.3	8.9	48.7	0.71 ± 0.01	15.1 ± 0.45	58.5 ± 0.02	6.30 ± 0.21
CA15-FTO	60.6	9.5	6.9	56.2	0.71 ± 0.01	16.4 ± 0.47	58.7 ± 0.02	6.90 ± 0.23

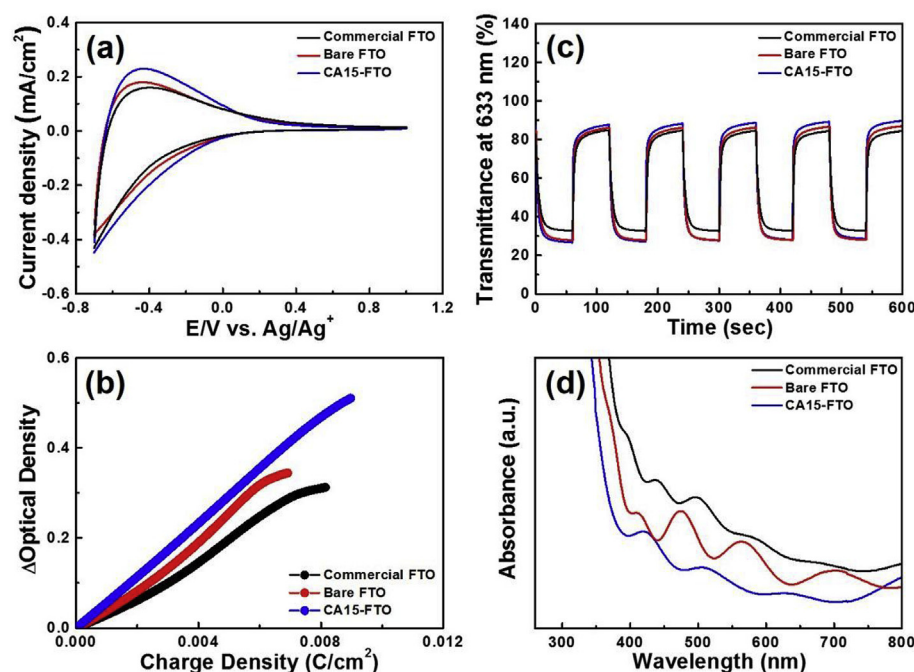


Fig. 6. (a) CV curves recorded in the potential range of -0.7 – 1.0 V at 20 mV/s in a three-electrode system, (b) *In situ* optical transmittances measured at -0.7 for colored state and 1.0 V for bleached state during 60 s, (c) OD curve at 633 nm as the result of applied charge density, and (d) absorption spectra of the samples composed of the FTO and WO_3 films measured in range from 260 to 800 nm.

the EC switching process [48,57]. In addition, the CE was considered to be a major factor to determine the EC performance, which was defined as the ratio of the changed optical density (ΔOD) at intercalated charge densities (Q/A) (see Eq. (10)) [58]:

$$\text{CE} = \Delta\text{OD}/(Q/A) = \log(T_b/T_c)/(Q/A) \quad (10)$$

where T_b and T_c are the transmittance value at the bleached and colored states, respectively. From the curve of ΔOD at the wavelength of 633 nm versus the applied potential of -0.7 V (see Fig. 6c), the calculated CE value was 39.4 cm^2/C for the commercial FTO, 48.7 cm^2/C for the bare FTO, and 56.2 cm^2/C for CA15-FTO. These results indicate that CA15-FTO has the highest CE value compared to the other two samples (the bare FTO and the commercial FTO). We assume that the enhancement of the CE value correlates with multifunctional effects of the combustion-activated FTO films increasing electron transfer efficiency caused by the (200) preferred orientations of the FTO and widening transmittance modulation resulting from the relaxation of interfacial scattering by a smooth and dense surface morphology of the FTO films (see Fig. 8).

Furthermore, to characterize the photovoltaic performances, we applied the FTO films as a TCO for the working electrode of the DSSCs. Fig. 7a shows the photocurrent–voltage (J – V) curves measured from the DSSCs with the commercial FTO, bare FTO, and CA15-FTO. The

resultant photovoltaic parameters of the DSSCs, such as open-circuit voltage (V_{oc}), short-circuit current density (J_{sc}), fill factor (ff), and photoconversion efficiency (PCE, η), are reported in Table 1. Of note, compared to other samples, CA15-FTO showed a superb PCE ($6.90 \pm 0.23\%$), which is 10% higher than that of the commercial FTO. This increase of PCE can be mainly related to a noticeably increased J_{sc} value in the event of no critical difference of V_{oc} and ff values. In the DSSCs, the lower sheet resistance of the FTO films to transfer photoelectrons and the higher light absorbance of the FTO films to excite the photoelectrons, the better the photovoltaic performance of the DSSC [18]. In our study, since the FTO films exhibited similar sheet resistance values among the samples, the improvement of J_{sc} value can be related to the amount of light entering the FTO films. Therefore, we measured the light absorbance using the half cells fabricated with the FTO films and TiO_2 with the dye (see Fig. 7b). The results showed that, compared to the bare FTO and the commercial FTO, the cells with CA15-FTO yielded an increased absorption in the range from 400 to 800 nm, which was caused by the highly enhanced transparency as the result of two main effects of the combustion-activated FTO films: relaxation of light scattering by a smooth and dense film structure of FTO and widening of the optical bandgap by decreased oxygen vacancies.

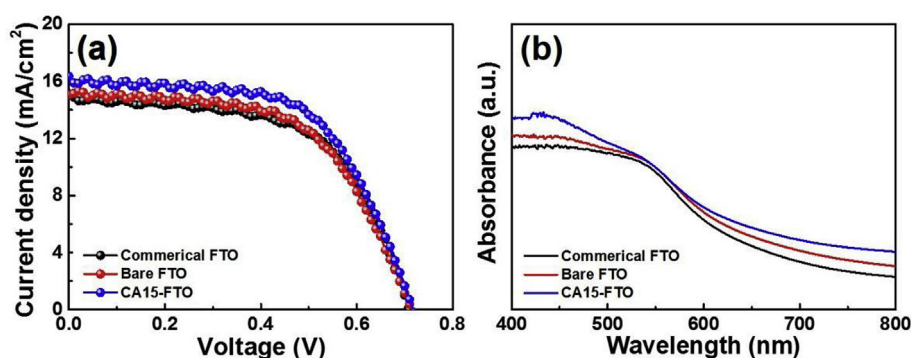


Fig. 7. (a) Photocurrent–voltage (J – V) curves measured from the DSSCs using the commercial FTO, bare FTO, and CA15-FTO as a TCO of working electrode and (b) absorption spectra of the half cells with the FTO films and TiO_2 with the dye.

Multifunctionality of combustion-activated FTO films for optoelectronic applications

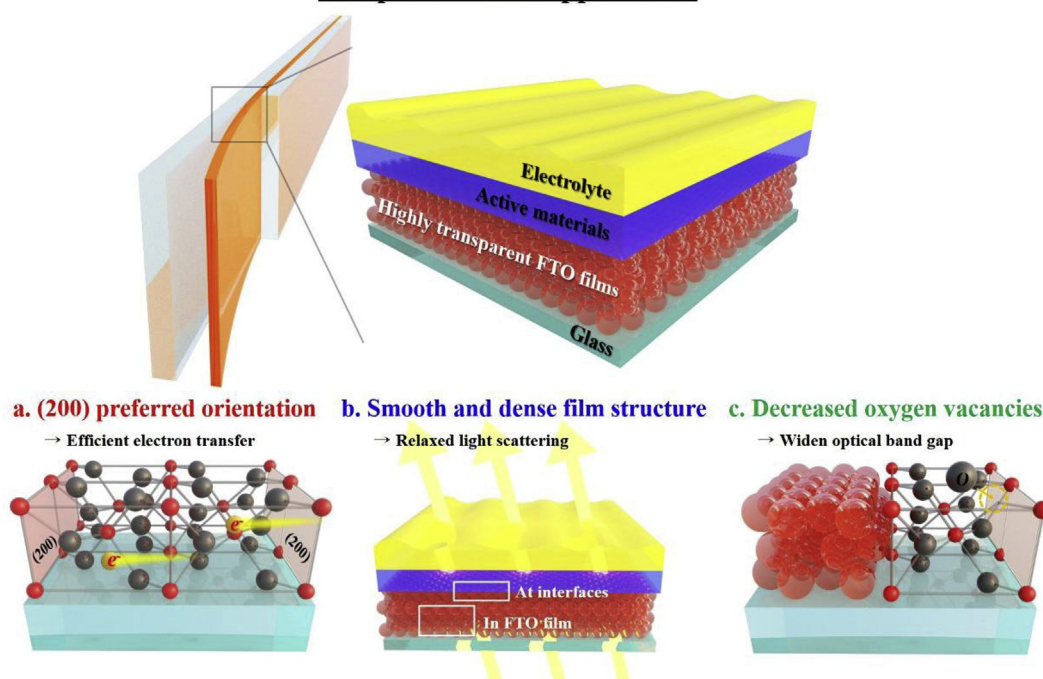


Fig. 8. Schematic illustration of multifunctional effects on combustion-activated FTO films for optoelectronic applications.

4. Conclusions

In sum, in the present study, we successfully achieved the development of combustion-activated pyrolysis route of the HUSPD to fabricate high-performance FTO films with high optical transparency. Compared to the basic route, due to the accelerated generation of self-generated energy with the optimized weight ratio of combustion activators, this route enables a significant formation of a smooth and dense film structure with the dominant (200) preferred orientation and reduction of the oxygen vacancies on the FTO films. As a result, the combustion-activated FTO films (CA15-FTO) exhibit superb FOM values ($5.34 \times 10^{-2} \Omega^{-1}$) with sheet resistance ($6.6 \pm 0.30 \Omega/\square$) and optical transmittance (90.1%), suggesting that their transparent conducting performances are superior to those of the other two samples (the commercial FTO and bare FTO) and previously reported results. Such excellent performance is mainly due to the improvement of the optical transmittance that results from the relaxation of light scattering on the surface by smooth and dense film structure and widening of the optical band gap by the decreased oxygen vacancies. More interestingly, our results demonstrate that the ECDs using CA15-FTO can improve the EC performance with CE and switching speed, which is caused from their multifunctional effects of efficient electron transfer caused by the (200) preferred orientations of the FTO and reduced interfacial scattering between TCO and EC materials induced by the smooth and dense surface morphology of the FTO films. In addition, when CA15-FTO was used as a TCO for the DSSCs, a significant improvement of photovoltaic performance was achieved due to the effect of the considerably improved transparency of the FTO films with decreased light scattering and a widened optical band gap. Therefore, we conclude that the proposed combustion-activated pyrolysis route of the HUSPD offers a novel and attractive strategy towards the development of multifunctional FTO films that would, in turn, enhance the performances of a wide variety of optoelectronic devices.

Acknowledgement

This study was supported by the Advanced Research Project funded by the SeoulTech (Seoul National University of Science and Technology).

Appendix A. Supplementary data

Supplementary data to this article can be found online at <https://doi.org/10.1016/j.ceramint.2019.02.080>.

References

- [1] R. Baetens, B.P. Jelle, A. Gustavsen, Properties, requirements and possibilities of smart windows for dynamic daylight and solar energy control in buildings: a state-of-the-art review, *Sol. Energy Mater. Sol. Cells* 94 (2010) 87–105.
- [2] H.-G. Im, B.W. An, J. Jin, J. Jang, Y.-G. Park, J.-U. Park, B.-S. Bae, A high-performance, flexible and robust metal nanotrough-embedded transparent conducting film for wearable touch screen panels, *Nanoscale* 8 (2016) 3916–3922.
- [3] P.-C. Chen, G. Shen, H. Chen, Y.-G. Ha, C. Wu, S. Sukcharoenchoke, Y. Fu, J. Liu, A. Facchetti, T.J. Marks, M.E. Thompson, C. Zhou, High-performance single-crystalline arsenic-doped indium oxide nanowires for transparent thin-film transistors and active matrix organic light-emitting diode displays, *ACS Nano* 3 (2009) 3383–3390.
- [4] J. Lee, B.-J. Jung, J.-I. Lee, H.Y. Chu, L.-M. Dob, H.-K. Shim, Modification of an ITO anode with a hole-transporting SAM for improved OLED device characteristics, *J. Mater. Chem.* 12 (2002) 3494–3498.
- [5] M.K. Ram, D.Y. Goswami, A. Takshi, E. Stefanakos, A new chromic (TouchChromic) thin film, *Acta Mater.* 121 (2016) 325–330.
- [6] N. Wan, J. Xu, G. Chen, X. Gan, S. Guo, L. Xu, K. Chen, Broadband anti-reflection and enhanced field emission from catalyst-free grown small-sized ITO nanowires at a low temperature, *Acta Mater.* 58 (2010) 3068–3072.
- [7] B.-R. Koo, H.-J. Ahn, Effect of hybrid nanoinks on solution-based Sn-doped In_2O_3 films under low-temperature microwave annealing, *Ceram. Int.* 42 (2016) 509–517.
- [8] H. Kim, R.C.Y. Auyeung, A. Piqué, Transparent conducting F-doped SnO_2 thin films grown by pulsed laser deposition, *Thin Solid Films* 516 (2008) 5052–5056.
- [9] A. Paoletta, C. Faure, V. Timoshevskii, S. Marras, G. Bertoni, A. Guerfi, A. Vijh, M. Armande, K. Zaghib, A review on hexacyanoferrate-based materials for energy storage and smart windows: challenges and perspectives, *J. Mater. Chem. A* 5 (2017) 18919–18932.
- [10] Z. Tong, S. Liu, X. Li, L. Mai, J. Zhao, Y. Li, Achieving rapid Li-ion insertion kinetics in TiO_2 mesoporous nanotube arrays for bifunctional high-rate energy storage smart

- windows, *Nanoscale* 10 (2018) 3254–3261.
- [11] S.-G. Park, C.W. Mun, M.K. Lee, T.Y. Jeon, H.-S. Shim, Y.-J. Lee, J.-D. Kwon, C.S. Kim, D.-H. Kim, 3D hybrid plasmonic nanomaterials for highly efficient optical absorbers and sensors, *Adv. Mater.* 27 (2015) 4290–4295.
 - [12] P. Somani, A.B. Mandale, S. Radhakrishnan, Study and development of conducting polymer-based electrochromic display devices, *Acta Mater.* 48 (2000) 2859–2871.
 - [13] Y. Yamada, H. Sasaki, K. Tajima, M. Okada, K. Yoshimura, Optical switching properties of switchable mirrors based on Mg alloyed with alkaline-earth metals, *Sol. Energy Mater. Sol. Cells* 99 (2012) 73–75.
 - [14] H. Park, D.S. Kim, S.Y. Hong, C. Kim, J.Y. Yun, S.Y. Oh, S.W. Jin, Y.R. Jeong, G.T. Kim, J.S. Ha, A skin-integrated transparent and stretchable strain sensor with interactive color-changing electrochromic displays, *Nanoscale* 9 (2017) 7631–7640.
 - [15] L. Chen, H. Deng, J. Tao, H. Cao, L. Sun, P. Yang, J. Chu, Strategic improvement of $\text{Cu}_2\text{MnSnS}_4$ films by two distinct post-annealing processes for constructing thin film solar cells, *Acta Mater.* 109 (2016) 1–7.
 - [16] R. Boppella, A. Mohammadpour, S. Illa, S. Farsinezhad, P. Basak, K. Shandar, S.V. Manorama, Hierarchical rutile TiO_2 aggregates: a high photonic strength material for optical and optoelectronic devices, *Acta Mater.* 119 (2016) 92–103.
 - [17] B.-R. Koo, H. An, H.-J. Ahn, High-surface area co-electrospun TiO_2 nanowires fabricated using shrinkage of polyvinylpyrrolidone for improved photovoltaic performance, *Ceram. Int.* 42 (2016) 1666–1671.
 - [18] J.-W. Bae, B.-R. Koo, H.-R. An, H.-J. Ahn, Surface modification of fluorine-doped tin oxide films using electrochemical etching for dye-sensitized solar cells, *Ceram. Int.* 41 (2015) 14668–14673.
 - [19] V. Consonni, G. Rey, H. Roussel, B. Doisneau, E. Blanquet, D. Bellet, Preferential orientation of fluorine-doped SnO_2 thin films: the effects of growth temperature, *Acta Mater.* 61 (2013) 22–31.
 - [20] C.K.T. Chew, C. Salcianu, P. Bishop, C.J. Carmalt, I.P. Parkin, Functional thin film coatings incorporating gold nanoparticles in a transparent conducting fluorine doped tin oxide matrix, *J. Mater. Chem. C* 3 (2015) 1118–1125.
 - [21] C.-H. Tsai, S.-Y. Hsu, T.-W. Huang, Y.-T. Tsai, Y.-F. Chen, Y.H. Jhang, L. Hsieh, C.-C. Wu, Y.-S. Chen, C.-W. Chen, C.-C. Li, Influences of textures in fluorine-doped tin oxide on characteristics of dye-sensitized solar cells, *Org. Electron.* 12 (2011) 2003–2011.
 - [22] N. Noor, I.P. Parkin, Enhanced transparent-conducting fluorine-doped tin oxide films formed by aerosol-assisted chemical vapour deposition, *J. Mater. Chem. C* 1 (2013) 984–996.
 - [23] T. Maruyama, H. Akagi, Fluorine-doped tin dioxide thin films prepared by radio-frequency magnetron sputtering, *J. Electrochem. Soc.* 143 (1996) 283–287.
 - [24] A. Nadarajah, M.E. Carnes, M.G. Kast, D.W. Johnson, S.W. Boettcher, Aqueous solution processing of F-doped SnO_2 transparent conducting oxide films using a reactive tin(II) hydroxide nitrate nanoscale cluster, *Chem. Mater.* 25 (2013) 4080–4087.
 - [25] J. Zhang, Y. Lou, M. Liu, H. Zhou, Y. Zhao, Z. Wang, L. Shi, D. Li, S. Yuan, High-performance dye-sensitized solar cells based on colloid-solution deposition planarized fluorine-doped tin oxide substrates, *ACS Appl. Mater. Interfaces* 10 (2018) 15697–15703.
 - [26] R. Otsuka, T. Endo, T. Takano, S. Takemura, R. Murakami, R. Muramoto, J. Madarász, M. Okuya, Fluorine doped tin oxide film with high haze and transmittance prepared for dye-sensitized solar cells, *Jpn. J. Appl. Phys.* 54 (2015) 08KF03.
 - [27] D.S. Bhachu, M.R. Waugh, K. Zeissler, W.R. Branford, I.P. Parkin, Textured fluorine-doped tin dioxide films formed by chemical vapour deposition, *Chem. Eur. J.* 17 (2011) 11613–11621.
 - [28] B.-R. Koo, D.-H. Oh, D.-H. Riu, H.-J. Ahn, Improvement of transparent conducting performance on oxygen-activated fluorine-doped tin oxide electrodes formed by horizontal ultrasonic spray pyrolysis deposition, *ACS Appl. Mater. Interfaces* 9 (2017) 44584–44592.
 - [29] A.I. Martínez, D.R. Acosta, Effect of the fluorine content on the structural and electrical properties of SnO_2 and ZnO-SnO_2 thin films prepared by spray pyrolysis, *Thin Solid Films* 483 (2005) 107–113.
 - [30] A.V. Moholkar, S.M. Pawar, K.Y. Rajpure, C.H. Bhosale, Effect of concentration of SnCl_4 on sprayed fluorine doped tin oxide thin films, *J. Alloy. Comp.* 455 (2008) 440–446.
 - [31] A.V. Moholkar, S.M. Pawar, K.Y. Rajpure, S.N. Almari, P.S. Patil, C.H. Bhosale, Solvent-dependent growth of sprayed FTO thin films with mat-like morphology, *Sol. Energy Mater. Sol. Cells* 92 (2008) 1439–1444.
 - [32] J. Wang, T.B. Daunis, L. Cheng, B. Zhang, J. Kim, J.W.P. Hsu, Combustion synthesis of p-type transparent conducting CuCrO_{2+x} and Cu:CrO_x thin films at 180 °C, *ACS Appl. Mater. Interfaces* 10 (2018) 3732–3738.
 - [33] A.G. Merzhanov, The chemistry of self-propagating high-temperature synthesis, *J. Mater. Chem.* 14 (2004) 1779–1786.
 - [34] M.-G. Kim, M.G. Kanatzidis, A. Facchetti, T.J. Marks, Low-temperature fabrication of high-performance metal oxide thin-film electronics via combustion processing, *Nat. Mater.* 10 (2011) 382–388.
 - [35] G.R.A. Kumara, C.S.K. Ranasinghe, E.N. Jayaweera, H.M.N. Bandara, M. Okuya, R.M.G. Rajapakse, Preparation of fluoride-doped tin oxide films on soda–lime glass substrates by atomized spray pyrolysis technique and their subsequent use in dye-sensitized solar cells, *J. Phys. Chem. C* 118 (2014) 16479–16485.
 - [36] X.-W. Hu, L. Li, B.-L. Gao, Z.-N. Shi, H. Li, J.-J. Liu, Z.-W. Wang, Thermal decomposition of ammonium hexafluoroaluminate and preparation of aluminum fluoride, *Trans. Nonferrous Metals Soc. China* 21 (2011) 2087–2092.
 - [37] L.C. Chen, F. Spaepen, Analysis of calorimetric measurements of grain growth, *J. Appl. Phys.* 69 (1991) 679–688.
 - [38] J. Sun, P. Sun, D. Zhang, J. Xu, X. Liang, F. Liu, G. Lu, Growth of SnO_2 nanowire arrays by ultrasonic spray pyrolysis and their gas sensing performance, *RSC Adv.* 4 (2014) 43429–43435.
 - [39] T.X. Phuoc, R.-H. Chen, Modeling the effect of particle size on the activation energy and ignition temperature of metallic nanoparticles, *Combust. Flame* 159 (2012) 416–419.
 - [40] D. Miao, Q. Zhao, S. Wu, Z. Wang, X. Zhang, X. Zhao, Effect of substrate temperature on the crystal growth orientation of SnO_2 :F thin films spray-deposited on glass substrates, *J. Non-Cryst. Solids* 36 (2010) 2557–2561.
 - [41] B. Thangaraju, Structural and electrical studies on highly conducting spray deposited fluorine and antimony doped SnO_2 thin films from SnCl_2 precursor, *Thin Solid Films* 402 (2002) 71–78.
 - [42] A. Smith, J.-M. Laurent, D.S. Smith, J.-P. Bonnet, R.R. Clemente, Relation between solution chemistry and morphology of SnO_2 -based thin films deposited by a pyrolysis process, *Thin Solid Films* 266 (1995) 20–30.
 - [43] A.E. Hassanien, H.M. Hashem, G. Kamel, S. Soltan, A.M. Moustafa, M. Hammam, A.A. Ramadan, Performance of transparent conducting fluorine-doped tin oxide films for applications in energy efficient devices, *Int. J. Thin. Fil. Sci. Tec.* 5 (2016) 55–65.
 - [44] C. Dong, X. Liu, X. Xiao, G. Chen, Y. Wang, I. Djerdj, Combustion synthesis of porous Pt-functionalized SnO_2 sheets for isopropanol gas detection with a significant enhancement in response, *J. Mater. Chem. A* 2 (2014) 20089–20095.
 - [45] A. Messad, J. Bruneaux, H. Cachet, M. Froment, Analysis of the effects of substrate temperature, concentration of tin chloride and nature of dopants on the structural and electrical properties of sprayed SnO_2 films, *J. Mater. Sci.* 29 (1994) 5095–5103.
 - [46] K. Murakami, I. Yagi, S. Kaneko, Oriented growth of tin oxide thin films on glass substrates by spray pyrolysis of organotin compounds, *J. Am. Ceram. Soc.* 79 (1996) 2557–2562.
 - [47] J.H. Park, S. Jang, D. Byun, J.K. Lee, Fluorine doped gallium tin oxide composite films as transparent conductive oxides on polyethylene terephthalate film prepared by electron cyclotron resonance metal organic chemical vapor deposition, *Thin Solid Films* 519 (2011) 6863–6867.
 - [48] J. Zhang, L. Gao, Synthesis of antimony-doped tin oxide (ATO) nanoparticles by the nitrate-citrate combustion method, *Mater. Res. Bull.* 39 (2004) 2249–2255.
 - [49] B.-R. Koo, D.-H. Oh, H.-J. Ahn, Influence of Nb-doped TiO_2 blocking layers as a cascading band structure for enhanced photovoltaic properties, *Appl. Surf. Sci.* 433 (2018) 27–34.
 - [50] T. Nikolay, L. Larina, O. Shevaleevskiy, B.T. Ahn, Electronic structure study of lightly Nb-doped TiO_2 electrode for dye-sensitized solar cells, *Energy Environ. Sci.* 4 (2011) 1480–1486.
 - [51] J. Jeong, S.-P. Choi, C.I. Chang, D.C. Shin, J.S. Park, B.-T. Lee, Y.-J. Park, H.-J. Song, Photoluminescence properties of SnO_2 thin films grown by thermal CVD, *Solid State Commun.* 127 (2003) 595–597.
 - [52] D.P. Queiroz, M.N. Pinho, Structural characteristics and gas permeation properties of polydimethylsiloxane/poly(propylene oxide) urethane/urea bi-soft segment membranes, *Polymer* 46 (2005) 2346–2353.
 - [53] H.A. Macleod, *Thin-film Optical Filters*, fifth ed., CRC Press, Florida, 2017.
 - [54] B.-R. Koo, H.-J. Ahn, Fast-switching electrochromic properties of mesoporous WO_3 films with oxygen vacancy defects, *Nanoscale* 9 (2017) 17788–17793.
 - [55] M. Wang, Q. Liu, G. Dong, Y. He, X. Diao, Influence of thickness on the structure, electrical, optical and electrochromic properties of AZO thin films and their inorganic all solid-state devices, *Electrochim. Acta* 258 (2017) 1336–1347.
 - [56] K.-H. Kim, B.-R. Koo, H.-J. Ahn, Sheet resistance dependence of fluorine-doped tin oxide films for high-performance electrochromic devices, *Ceram. Int.* 44 (2018) 9408–9413.
 - [57] C. Yan, W. Kang, J. Wang, M. Cui, X. Wang, C.Y. Foo, K.J. Chee, P.S. Lee, Stretchable and wearable electrochromic devices, *ACS Nano* 8 (2014) 316–322.
 - [58] S.I. Noh, H.-J. Ahn, D.-H. Riu, Photovoltaic property dependence of dye-sensitized solar cells on sheet resistance of FTO substrate deposited via spray pyrolysis, *Ceram. Int.* 38 (2012) 3735–3739.